Nanoscale Advances

ROYAL SOCIETY OF CHEMISTRY

PAPER

View Article Online
View Journal | View Issue



Cite this: *Nanoscale Adv.*, 2024, **6**, 5925

# Synergistic effect of Zn-$AgIn_5S_8$/CdS Z-scheme heterojunction and S-doped rGO for efficient removal of chromium from contaminated water

Soumya Mishra,[a] Naresh Kumar Sahoo, *[a] Prasanta Kumar Sahoo,[b] Satyanjib Sahoo,[a] Prangya Ranjan Rout[c] and Goutam Rath[d]

This study aimed to synthesize a Zn-$AgIn_5S_8$/CdS/SrGO nanocomposite for Cr(VI) removal from contaminated water under solar irradiation. To prevent photo corrosion of CdS, a Z-scheme heterojunction was formed between CdS and Zn-$AgIn_5S_8$. The introduction of $Ag^{2+}$ plasmonic materials extended the light absorption range and stabilized the photocatalyst. Further, to improve the catalytic surface area, electrical conductivity, and minimize the rate of electron and hole pair recombination, the Zn-$AgIn_5S_8$/CdS Z-scheme heterojunction was loaded onto S-doped rGO. The morphological and structural analysis of the synthesized nanomaterials (NMs) was done using various techniques, including XRD, FT-IR, UV-vis DRS, FESEM, TEM, EDAX, photoluminescence, and Raman spectroscopy. Results revealed that the Zn-$AgIn_5S_8$/CdS/SrGO nanocomposite removed 85% of Cr(VI) at an initial concentration of 50 mg $L^{-1}$ in 180 min when exposed to solar irradiation. The simulated first-order kinetic model fitted to the experimental data for Cr(VI) reduction by the nanocomposite exhibits a high correlation coefficient ($R^2 \geq 0.97$) and the $K_{app}$ value for Zn-$AgIn_5S_8$/CdS/SrGO ($K_{app} = 0.0114$ $min^{-1}$) is around 1.6 times larger than that of bare $ZnAgIn_5S_8$. Moreover, Zn-$AgIn_5S_8$/CdS/SrGO heterojunctions show excellent reusability up to 4 cycles. Further, the possible photocatalytic mechanism of Cr(VI) reduction has been proposed. Therefore, the Zn-$AgIn_5S_8$/CdS/SrGO nanocomposite could serve as an alternative photocatalyst system driven by solar light for Cr(VI) reduction.

Received 25th April 2024
Accepted 10th September 2024

DOI: 10.1039/d4na00350k

rsc.li/nanoscale-advances



## 1. Introduction

Industrial effluents containing heavy metals are the major contributors to water pollution.[1] Cr(VI) ranked third among the common toxic environmental pollutants discharged from several industrial wastewaters such as textile, electroplating, nuclear power plants, leather tanning, dying, and photography industries.[2] Due to increased industrial use, the concentration of chromium in wastewater typically ranges from 10 to 100 mg $L^{-1}$.[3] Chromium primarily exists in the environment in the form of Cr(III) and Cr(VI). Cr(VI) compounds are carcinogenic, cause tissue damage and dermatitis, and are 10 to 1000 times more toxic than Cr(III) compounds.[1,4] However, the permissible upper limit for Cr(VI) in the environment is 0.05 mg $L^{-1}$.[5] In contrast, Cr(III) indicates reduced mobility compared to Cr(VI) and is not soluble in water. Additionally, it readily undergoes hydrolysis to produce insoluble chromium hydroxides and is removed from the contaminated water.[3,5] Therefore, converting highly toxic Cr(VI) into non-toxic Cr(III) represents a viable strategy for eliminating Cr(VI) from contaminated environments.

Various traditional techniques are available for addressing the removal of Cr(VI) from contaminated environments including solvent extraction, membrane separation, coagulation, flocculation, and the electrolysis process.[6] Among them, photocatalysis is considered to be the most promising technique because of numerous advantages, such as being cost-effective, and efficient, not producing secondary products, and having an eco-friendly nature compared to traditional approaches.[7,8] However, photocatalysts have some limitations, including unsuitable conduction and valence bands, photo-induced charge carrier recombination, restricted surface area, and limited visible light absorption capacity, which affect the overall photocatalytic efficiency. Modifications like defect alterations, adding active sites, and heterojunction formation can be applied to address these limitations. Photocatalytic reduction of Cr(VI) requires photocatalysts with redox properties, but designing such photocatalysts is still a significant

[a]*Department of Chemistry, Environmental Science and Technology Program, Faculty of Engineering and Technology (ITER), Siksha 'O' Anusandhan (Deemed to be University), Bhubaneswar 751030, Odisha, India. E-mail: nareshsahoo@soa.ac.in; nareshks2010@gmail.com*

[b]*Environmental Hydrology Division, National Institute of Hydrology, Jalvigyan Bhawan, Roorkee 247667, India*

[c]*Department of BioTechnology, Dr B R Ambedkar National Institute of Technology Jalandhar, India*

[d]*School of Pharmaceutical Sciences, Siksha 'O' Anusandhan (Deemed to be University), Bhubaneswar 751030, Odisha, India*

challenge.[9] In recent years, metal chalcogenides I–III–VI QDs, such as ZnS-$AgInS_2$, $CuIn_{1-x}$ $GaxS_2$, and $CuGa_2In_3S_8$ are widely popular for the degradation of organic pollutants because they possess a large surface area, narrow band gap, more negative CB sites, good carrier mobility and a broad light absorption range.[10,11] In addition to adjusting the composition and size of I–III–VI QD photocatalysts, a significant amount of research has focused on creating heterostructured photocatalysts, including $AgIn_5S_8/TiO_2$, $AgIn_5S_8/AgInS_2$, Zn-$AgIn_5S_8$/ZnS, and Zn-$AgIn_5S_8$/$MoS_2$.[12] This indicates a promising future for photocatalytic applications through careful composition and structure design.[13] Liu *et al.*[14] reported that in photocatalytic applications, enhancing Ag-In-S-based QDs primarily focuses on adjusting the ratios of different elements to decrease the bandgap, thereby increasing visible light absorption. Zhang *et al.*[15] fabricated a 0D/2D $\alpha$-$Fe_2O_3$/Zn-$AgIn_5S_8$ Z-scheme heterostructure for the $H_2$ generation under the illumination of the sun. The application of $\alpha$-$Fe_2O_3$ with superior conductivity enhances the mobility of the charge carrier and inhibits the electron and hole pair recombination. In addition, a homogenous distribution of 0D Zn-$AgIn_5S_8$ QDs on $\alpha$-$Fe_2O_3$ is produced by the extraordinarily close interface contact between $\alpha$-$Fe_2O_3$ and Zn-$AgIn_5S_8$ due to electrostatic adsorption caused by the zeta potential difference, which inhibits QD agglomeration.

Nevertheless, $AgIn_5S_8$ QDs surface defects resulting from unsaturated surface atom bonding prevent photo-induced charge carriers for photocatalytic reactions and give rise to non-radiative recombination.[11,16] In addition, these I–III–VI NCs still suffer from the stability of sulfide materials and thus, limit their application.[17] Recently, researchers have devised a range of techniques such as element doping, surface structure optimization, co-catalyst loading, and heterojunction construction to enhance the catalytic performance and stability of QDs.[15] Thus, in the present study, to overcome these limitations, a Z-scheme heterojunction was constructed between CdS and Zn $AgIn_5S_8$. It has been reported that the expansion of the light absorption range and stability of the $\beta$-$In_2S_3$ photocatalyst can be significantly improved by incorporating $Cu^{2+}$ into the $\beta$-$In_2S_3$.[18] Thus, in the present study, Zn was doped to $In_2S_3$ to prevent charge pair recombination. The introduction of $Ag^{2+}$ plasmonic materials extended the light absorption range and stabilized the photocatalyst.[15]

Among the various photocatalysts, CdS is a promising candidate due to its narrow bandgap energy of 2.4 eV and very high quantum yield.[8] Overall, CdS is easy to prepare, inexpensive, and its morphology can be controlled. It is highly effective for visible light, making it one of the most notable visible-light-responsive photocatalysts among sulfides for photocatalytic applications.[19] Yang *et al.*[20] used CdS in CdS/(I/S) composites Illite/Smectite (I/S) clays for Cr(VI) reduction, achieving an impressive 90.6% reduction of 20 mg $L^{-1}$ Cr(VI). However, the primary constraints of the CdS photocatalytic system include two main issues: First, CdS tends to aggregate into larger particles, which significantly reduces the specific surface area and has a high rate of photogenerated charge carrier recombination.[21] Secondly, the formation of holes in the VB of the semiconductor is the primary cause of the instability and photocorrosion of the CdS photocatalyst. Therefore, a special design of hole transfer is highly needed, such as the incorporation of hole-scavenging agents[8] and the fabrication of a Z-scheme heterojunction.[15] For instance, among the heterojunctions, the Z-scheme heterojunction stands out as an effective approach with superior redox capacity to overcome the constraints of unmodified photocatalysts.[22] Thus to overcome this above-mentioned limitation a Z-scheme heterojunction was proposed between $ZnAgIn_5S_8$ and CdS photocatalyst. Further, the stability of the CdS NPs has been improved using 3 mercaptopropionic acid.[8]

The primary goal of photocatalyst design is to promote the separation and transfer of photoinduced electron and hole pairs, for which co-catalyst loading is crucial.[17] Gong *et al.*[17] fabricated $MoS_2$-modified Zn-$AgIn_5S_8$ solar-driven QDs for the degradation of rhodamine B and tetracycline, where $MoS_2$ acts as a cocatalyst to accelerate electron mobility from $AgIn_5S_8$ QDs. Similarly, Yang *et al.*[12] synthesized Zn-$AgIn_5S_8$ QDs on g-$C_3N_4$ to produce 0D/2D heterojunction photocatalysts, wherein g-$C_3N_4$ nanosheets act as charge transfer mediators. Zhang *et al.*[10] synthesized 0D/2D Zn-$AgIn_5S_8$ heterojunction using NiS as a co-catalyst, which offers adequate active sides and facilitates efficient charge transfer, resulting in 5200 μmol $g^{-1}$ $h^{-1}$, which is 11 times higher than pure $AgIn_5S_8$QDs. As per a recent study, reduced graphene oxide (rGO) is becoming increasingly popular as a co-catalyst because of its remarkable attributes, which include an extensive specific surface area (measuring at 2600 $m^2$ $g^{-1}$), strong thermal and chemical stability, superior electron conductivity (reaching 15 000 $m^2$ $v^{-1}$ $s^{-1}$), high density of functional groups, as well as being an excellent choice for a carrier or promoter of catalysts.[23] Recent research suggests that the electrical and chemical reactivity of rGO can be enhanced by introducing vacancy defects, adding heteroatoms, and non-metal doping.[24,25] Specifically, introducing heteroatoms into the material effectively enhanced the number of active sites and controlled the distribution of electrons.[26] Furthermore, there is a growing interest in S-doped graphene-based materials, mainly due to the broader band gap resulting from the electron-withdrawing character of S[16].[27] Xuan *et al.*[9] reported using rGO in the rGO-CdS-MnOx (GCM) nanocomposite, highlighting its suitability as a co-catalyst in photocatalysis due to its strong electron capture ability, low cost, and high specific surface area. Thus in the present study S-doped r-GO was used as a co-catalyst and acted as a charge transfer mediator that promotes the electron transfer.

The main objective of this study was to prepare a low-cost Zn-$AgIn_5S_8$/CdS/SrGO photocatalytic nanocomposite by hydrothermal procedure for the removal of Cr(VI) from contaminated water. The morphological, structural, and compositional characterizations of the NMs were carried out by XRD, FT-IR, UV-vis, DRS, FESEM, TEM, EDAX, PL, and Raman spectroscopy analysis. The photocatalytic Cr(VI) reduction performance of the nanocomposite was evaluated, and the effects of different parameters such as photocatalyst dose, irradiation time, and initial concentration of Cr(VI) were studied. The reduction of Cr(VI) using the nanocomposite was evaluated by applying various kinetic models. The photocatalytic adsorption and Cr(VI)

reduction mechanisms were fundamentally elucidated. Further, the reusability of the nanocomposite for synergistic adsorption and reduction of Cr(VI) removal was investigated.

## 2. Experimental section

### 2.1. Materials

Analytical-grade potassium dichromate was purchased from SRL, India (purity 99.5%). Isopropanol (purity 99.5%), 3-mercaptopropionic acid (purity 99%), and L-Cysteine (purity 99%) were purchased from Hi-Media, India. Indium oxide (purity 99.5%) was purchased from Burgoyne Burbidges and Co., India. Cadmium chloride (purity 99%), silver nitrate (purity 98%), zinc acetate (purity 99.5%), graphite powder (purity 98%), and hydrazine hydrate (purity 80%) were purchased from Merck, India. Disodium sulphide (purity 60%) was purchased from LOBA Chem, India. All other reagents and chemicals were of analytical and laboratory grade.

### 2.2. Methods

**2.2.1. Synthesis of Zn-$AgIn_5S_8$.** Zn-$AgIn_5S_8$ QDs were synthesized using a simple hydrothermal method according to reported literature[17] with some modifications. First, 0.1728 g of $AgNO_3$, 1.947 g of $In_2O_3 \cdot 5H_2O$ and 1.947 g of $Zn(OAc)_2 \cdot 2H_2O$ (serving as the metal precursors) were dissolved in 24 ml of deionized water containing 1.09 g of L-cysteine (as a protective agent). After subjecting the mixture to ultra-sonication for 15 minutes, the pH was adjusted to 8.5 using a 1.0 M NaOH solution. Subsequently, the mixture was stirred for 20 minutes. The resulting solution was then transferred to a 100 ml autoclave made of Teflon-lined stainless steel and held at a temperature of 110 °C for 4 h. The sample was collected through centrifugation at 12 000 rpm for 15 min, and the obtained precipitate was washed three times with a mixture of deionized water and ethanol and re-suspended in deionized water for subsequent use.

**2.2.2. Synthesis of pure CdS.** CdS was synthesized as described in the literature.[8,28] Briefly, 1st solution was prepared by dissolving 2.7 g of Cd $(NO_3)_2$ in 15 ml of isopropanol. Then, 3.71 ml of MPA (Mercaptopropionic acid) capping agent was added, and the pH was fixed at 10.5 by adding 3 M NaOH. The resulting suspension was purged with nitrogen gas for 15 min. A 2nd solution was prepared by dissolving 0.652 g $Na_2S$ in 60 ml of isopropanol. The suspension was vigorously stirred for 2 h. Then, the 1st solution was dripped into 2nd solution under vigorous stirring at room temperature. The aging of the solution was done for 8 h at 37 °C. The suspension was transferred into an autoclave at 180 °C for 24 h. The resulting suspension was centrifuged at 12 000 rpm for 15 min, and the precipitate was washed with water and ethanol three times. The final product was dried in the oven at 90 °C for 6 h.

**2.2.3. Synthesis of SrGO.** Sulfur-doped graphene oxide was synthesized using the modified Hummers' method.[23,29] Briefly, 2 g of graphite powder was added to 80 ml of concentrated $H_2SO_4$ in an ice bath at 0 °C. Then 4 g $NaNO_3$ and 8 g $KMnO_4$ were added gradually under stirring, and the mixture temperature was kept below 10 °C for 4 h. After that, the mixture was stirred at 35 °C for another 4 h, then diluted with 200 ml of deionized water, and stirred again for 1 h. The reaction was terminated by adding 15 ml of a 30% $H_2O_2$ solution. The solid product was separated by centrifugation at 12 000 rpm for 20 min. The centrifuged precipitate was washed several times with water and absolute ethanol to remove any impurities. The final product was then dried in a vacuum oven at 50 °C for 24 h to obtain GO. To synthesize SrGO, 1 g of this synthesized GO was sonicated with 300 ml of distilled water for 20 min. Nitrogen gas was purged into the solution for 15 min. Then 0.5 ml of hydrazine hydrate solution was added and sonicated for 10 min. After that, 3 g of $Na_2S$ was added to the reaction mixture as a sulfur precursor. The resultant suspension was transferred to a reflux condenser and refluxed at 80 °C for 8 h. The resulting suspension was centrifuged at 12 000 rpm for 15 min. The obtained precipitate was repeatedly washed with distilled water and ethanol, followed by drying at 65 °C in a vacuum oven to get the end product.

**2.2.4. Preparation of Zn-$AgIn_5S_8$/CdS/SrGO nanocomposite.** Zn-$AgIn_5S_8$/CdS/SrGO nanocomposite was synthesized by the hydrothermal method, which is represented in Scheme 1. 0.095 g of Ag $(NO_3)_2$, 0.471 g of $In_2O_3 \cdot 5H_2O$ and 0.186 g of $Zn(OAC)_2 \cdot 2H_2O$ were dissolved in 20 ml of deionized water. Then 0.36 g of L-cysteine was added and sonicated for 15 min. The pH of the reaction mixture was adjusted to 8.5 with a 0.5 M NaOH solution. Then 500 mg of previously synthesized CdS and 1 g of previously prepared SrGO were added to the suspension under continuous stirring, and the pH was further adjusted to 8.5. The suspension was transferred into an autoclave at 110 °C for 4 h. The resultant suspension was centrifuged at 12 000 rpm for 15 min, the precipitate was washed three times with ethanol and distilled water, and the final product was dried in a desiccator.

### 2.3. Experimental setup

The performance of the synthesized nanoparticles for the photoreduction of Cr(VI) was carried out under solar light illumination. In this experiment, 25 ml of Cr(VI) solutions with varying concentrations of 25, 30, 40, and 50 mg $L^{-1}$ were placed into 4 different conical flasks. Subsequently, each flask underwent a 20 minutes nitrogen purge to eliminate dissolved oxygen. Then 1 g $L^{-1}$, of Zn-$AgIn_5S_8$/CdS/SrGO nanocomposite was added to each flask, and again nitrogen gas was purged inside the solution to remove the rest of the dissolved oxygen present in it. In a separate conical flask, a control experiment was conducted with a 40 mg $L^{-1}$ Cr(VI) solution without adding the nanocomposite. The experiment was conducted in a dark condition with constant stirring at 300 rpm for 15 min, and then the photocatalytic reaction was performed under solar light irradiation. Samples were collected at regular intervals of time from each flask and centrifuged at 12 000 rpm for 20 min. The collected supernatant was used to determine the residual concentration of Cr(VI). The concentration of remaining Cr(VI) was estimated by a colorimetric technique using a diphenylcarbazide (DPC) solution as depicted in APHA.[30]

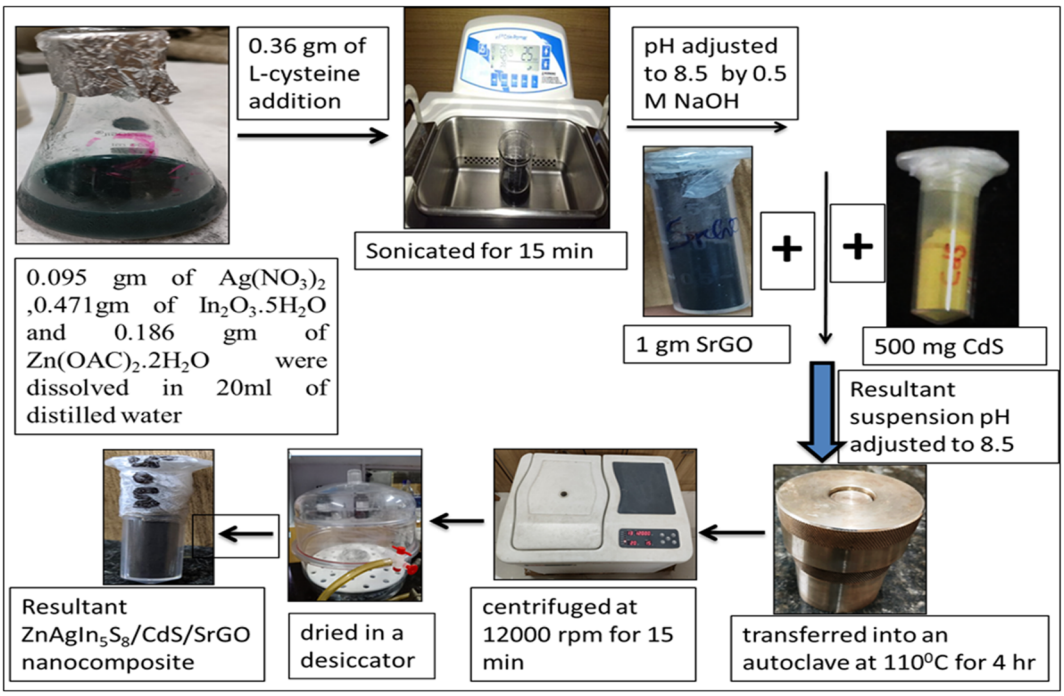


Scheme 1 Schematic illustration of the synthesis of Zn-$AgIn_5S_8$/CdS/SrGO nanocomposite.

### 2.4. Analytical methods

In this current investigation, X-ray diffraction (XRD) analysis was conducted utilizing an X-ray powder diffractometer (Model: Rikagu Ultima Japan) equipped with a CuK$\alpha$ ($\lambda = 1.5405$ Å) X-ray source. The study encompassed a broad spectrum of Bragg's angles (ranging from 20° to 80°) to validate the formation of the desired material. The crystal structure, unit cell parameters, and Miller indices were determined by utilizing the computer software program X'Pert High Score Plus. Using a Varian spectrophotometer (Jasco FT/IR-4600 LE, Japan) FTIR analysis was conducted to examine the molecular vibrations of the NMs and identify their functional groups. The optical absorbance liquid samples were assessed through a UV/visible spectrophotometer Evolution 220, Thermo Scientific, USA. Additionally, a Renishaw Invia Raman microscope (make: UK) with a green 532 nm laser was used to determine the various vibrational modes linked to the synthesized NM samples. To assess the recombination of electron and hole, the NMs were analyzed by photoluminescence (PL) spectroscopy at various excitation wavelengths, such as 488 nm, 532 nm, 633 nm, and 785 nm. These measurements were conducted using the (FLS 1000 photoluminescence spectrophotometer, Edinburgh). A FE-SEM (a Gemini SEM 450 instrument, Germany) equipped with Tungsten and $LaB_6$ filaments as the light source was used to analyze the morphological characteristics of the NMs. Elemental composition was determined through an energy-dispersive X-ray spectroscopy (EDS) system integrated with the FESEM (a Gemini SEM 450 instrument). The analysis was conducted in plain-view mode, employing a 10 kilovolt electron beam. K$\alpha$ and L$\alpha$ energy values were established for all materials. TEM investigation was performed using FEI Tecnai G2 20 S-TWIN with a carbon-coated copper grid with a mesh size of 200 nm. A Jasco V 770 UV-Visible Diffuse Reflectance Spectrophotometer (UV-Vis DRS), Japan was employed to determine the optical absorbance and bandgap energy of the synthesized Solid NMs. The band gap energy of the synthesized NMs was determined using eqn (1). The band gap energy of the synthesized NMs was approximated using Tauc's equation, as shown in eqn (2).

$$E_g(\text{eV}) = \frac{1240}{\lambda_G} \quad (1)$$

$$\alpha h\nu^{1/\gamma} = B(h\nu - E_g) \quad (2)$$

where $h$ is the Planck constant, $\nu$ is the frequency of the photon, $E_g$ is the band gap energy, and $B$ is a constant. The $\gamma$ factor depends on the nature of the electron transition and is equal to 2 or 1/2 for the direct and indirect transition band gaps, respectively.[31]

## 3. Results and discussion

### 3.1. Characterization of synthesized nanocomposite

**3.1.1. XRD study of the synthesized nanocomposite.** The X-ray diffraction pattern of synthesized Zn-$AgIn_5S_8$, CdS, SrGO, and Zn-$AgIn_5S_8$/CdS/SrGO nanocomposite are demonstrated in Fig. 1. The Zn-$AgIn_5S_8$ diffraction peaks at 2$\theta$ values of 21.51°, 25.0°, 26.6°, 28.4°, 30.65°, 35.35°, 44.5°, 48.0°, 51.9°, and 60.78° correspond to the (111), (120), (002), (211), (130), (121), (320), (123), and (042) crystal planes, revealing its orthorhombic phase with JCPDS No. 03-065-7332. This observation is correlated with the reported literature.[14] The CdS diffraction peaks at 2$\theta$ values of 25.04°, 26.37°, 44.09°, and 48.07° indexed as (100), (002),

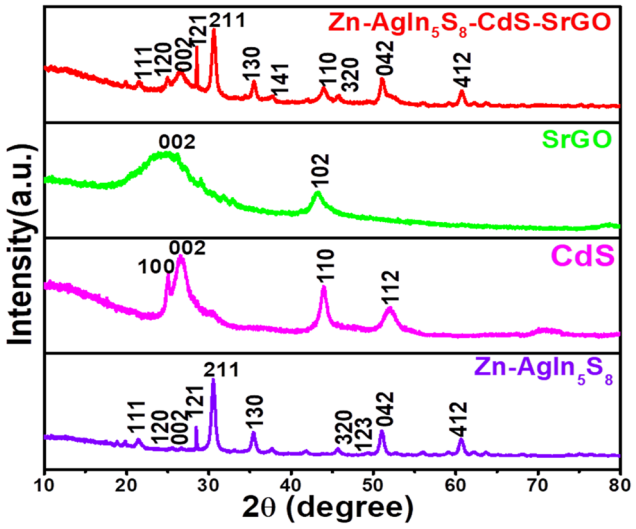


Fig. 1 XRD patterns of the prepared Zn-$AgIn_5S_8$, CdS, SrGO, Zn-$AgIn_5S_8$/CdS/SrGO NMs.

(110), and (112) crystal planes, respectively, which is in good agreement with JCPDS No. 00-041-1049. This indicates the hexagonal wurtzite phases of synthesized CdS, as similar observations have also been reported in many reports in the literature.[32,33] The absence of any other impurity peaks suggests the formation of a high-purity CdS nanostructure. Further, the clearly defined peaks indicate a well-developed crystal structure of the synthesized nanomaterials. A strong and narrow diffraction peak at a $2\theta$ value of 26.37° corresponding to the (002) plane indicates preferential growth along [001] hexagonal CdS crystallites.[32] The diffraction peaks at $2\theta$ values of 26.16° and 43.09° of SrGO correspond to (002) and (102) planes, respectively, matched with JCPDS No. 01-075-1621 and 00-026-1075. This peak has maximum intensity at a diffraction angle of ~26.16°, corresponding to the characteristic (002) reflection, which indicates the presence of parallel graphene layers in the structure of SrGO, similar observation has also been reported in the literature.[34] The diffraction peaks of $ZnAgIn_5S_8$/CdS/SrGO nanocomposite at $2\theta$ values of 21.60°, 24.96°, 26.63°, 28.51, 30.59°, 35.51°, 37.78°, 43.93°, 45.69°, 51.07°, and 60.70° correspond to (111) (120) (002) (121) (211) (130) (141) (110) (320) (042) and (412) planes (JCPDS No. 03-065-7332 and 00-041-1049), respectively. In the same $2\theta$ position (~30.2°), a sharp peak was observed both in Zn-$AgIn_5S_8$ and Zn-$AgIn_5S_8$/CdS/SrGO nanocomposite which indicates the (211) plane. Also, a broad peak (~26°) was observed in both CdS (002 crystal plane) and Zn-$AgIn_5S_8$/CdS/SrGO nanocomposite, which indicates that both Zn-$AgIn_5S_8$ and CdS have been successfully grown on the SrGO surface. The Williamson and Hall (W–H) equation is used to estimate both the average crystalline size and lattice strain. The linear form of the W–H equation is shown as follows:

$$\beta\cos\theta = 4\sin\theta + \frac{K\lambda}{D} \quad (3)$$

where $\beta$ represents the full-width half maxima (FWHM), the angle of diffraction is denoted by $\theta$, $D$ stands for average crystalline size, and $\lambda$ represents the wavelength value of 0.154 nm, K which is constant with a value of 0.89. The plot between 4 sin $\theta$ *versus* $\beta$ cos $\theta$ was constructed where the slope of the linear plot represents the lattice strain and the *Y*-intercept gives the average crystalline size. In this work, the average crystalline sizes of Zn-$AgIn_5S_8$, CdS, SrGO, and Zn-$AgIn_5S_8$/CdS/SrGO nanocomposite were calculated to be 16 nm, 2.52 nm, 2.39 nm, and 10.51 nm, respectively.

**3.1.2. FT-IR analysis of the synthesized nanocomposite.** To assess the different functional groups and covalent bonding patterns of the synthesized NMs were characterized using the FTIR analysis technique. Fig. 2(a) demonstrates the FTIR spectra of Zn-$AgIn_5S_8$, the appearance of a peak at 1395 $cm^{-1}$ indicates the presence of In–S bond which is well correlated with reported literature in the range of 1300 to 1550 $cm^{-1}$.[35] The stretching modes of C–C are observed at 1089.58 $cm^{-1}$.[36] The peaks above 3000 $cm^{-1}$ indicate the presence of the OH group, which is well-matched with the FTIR data reported in many works of literature.[37,38] In Fig. 2(b), depicting the FTIR spectrum of CdS, a solitary peak appears at 3395.07 $cm^{-1}$, attributed to the O–H stretching vibration of absorbed water molecules.[39] The presence of this peak may be indicative of moisture within the sample. Another peak at 512.97 $cm^{-1}$ suggests the stretching of Cd–S bonds in CdS nanoparticles. However, the peak at 512.97 $cm^{-1}$ appears relatively weak due to the presence of moisture in the sample. Additionally, strong absorption bands appear at 1000.87 $cm^{-1}$ indicating the presence of faint traces of sulphur–oxygen (SO) bonds in the CdS sample.[40] Furthermore, a moderately intense band at 1541.81 $cm^{-1}$ could be attributed to the stretching vibrations of sulfate groups.[41] Normally, the Cd–S stretching band occurs in the lower wavenumber region, *i.e.*, below 700 $cm^{-1}$. A medium-strong absorption peak at 650.858 $cm^{-1}$ corresponds to the Cd–S stretching mode, and similar observations have also been reported in the literature.[42] Fig. 2(c) represents the FTIR spectra of SrGO. The peak at 1697.05 $cm^{-1}$ of SrGO is due to C=C stretching vibration. Similarly, a strong peak at 2359.48 $cm^{-1}$ is due to the O=C=O stretching mode, which indicates the presence of oxygen in the SrGO sample. The appearance of a peak at 3564.77 $cm^{-1}$ is due to the presence of the O–H group.[43] The FTIR spectra of the Zn-$AgIn_5S_8$/CdS/SrGO nanocomposite is shown in Fig. 2(d). The presence of a peak at 495.616 $cm^{-1}$ shows Cd–S bond stretching.[40] The peak at 1337.39 $cm^{-1}$ corresponds to the C–O stretching of SrGO. The peak at 1697.05 $cm^{-1}$ occurs due to C=C stretching vibration. A strong peak at 2341.16 $cm^{-1}$ is due to O=C=O stretching, which indicates the presence of oxygen in the SrGO sample. The stretching modes of C–C are observed at 1089.58 $cm^{-1}$. The appearance of a peak at 1395 $cm^{-1}$ indicates the presence of In–S bond in the nanocomposite. These results have authenticated that the Zn-$AgIn_5S_8$/CdS/SrGO nanocomposite has been well synthesized.

**3.1.3. UV-vis DRS study of the synthesized nanocomposite.** UV-visible diffuse reflectance spectroscopy (UV-vis DRS) was employed to investigate the optical behavior of the photocatalysts.[25] Fig. 3(a) presents the UV-vis DRS spectra of the synthesized nanomaterials. A bathochromic shift (redshift) is observed with the formation of the Zn-$AgIn_5S_8$/CdS/SrGO

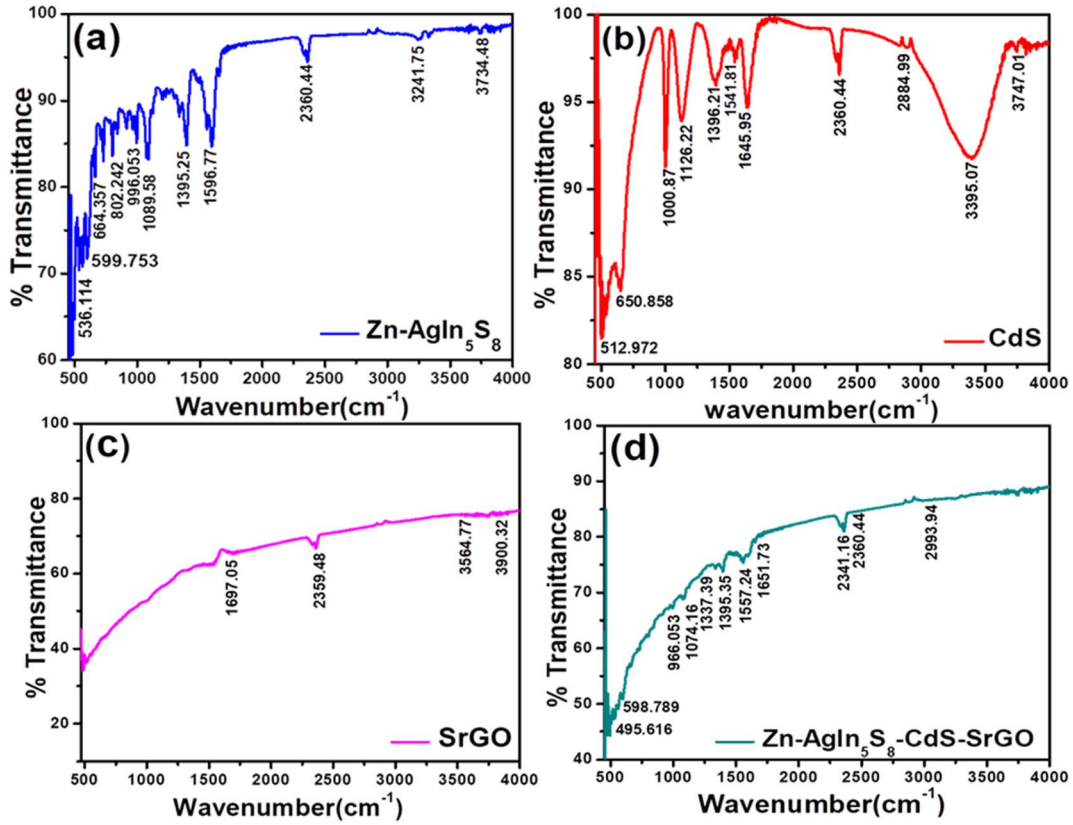


Fig. 2 FTIR study of (a) of Zn-$AgIn_5S_8$ (b) CdS (c) SrGO and (d) Zn-$AgIn_5S_8$/CdS/SrGO nanocomposite.

nanocomposite compared to individual Zn-$AgIn_5S_8$, S-rGO and CdS NMs. The band gap energy of the synthesized NMs was determined using the Tauc plot, as shown in Fig. 3(c)–(f). Fig. 3(c) represents the UV-vis DRS Tauc plot of Zn-$AgIn_5S_8$ NM with computed band gap energy of 2.05 eV. Similarly, for CdS nanoparticles, the estimated band gap energy is 2.28 eV, as depicted in Fig. 3(d). This finding aligns with the values reported in the literature.[44] The band gap energy of SrGO was also calculated using the Tauc plot, as shown in Fig. 3(e). Following rGO functionalization, the band gap energy exhibited a slight increase from 0.95 eV to 1.37 eV for SrGO, suggesting that the optical characteristics of rGO underwent alteration upon chemical modification with sulfate groups, which nearly matched the referenced data in the literature.[45] When comparing the band gap energies of the individual NMs, namely $ZnAgIn_5S_8$ (2.05 eV), CdS (2.28 eV), and SrGO (1.37 eV), it is evident that the Zn-$AgIn_5S_8$/CdS/SrGO nanocomposite exhibits a significant red shift toward the visible spectrum, featuring a notably reduced band gap energy of approximately 1.31 eV, as illustrated in Fig. 3(d). This red shift towards lower energy levels in the synthesized nanocomposite enhances its reactivity to visible light, signifying its potential for efficient utilization of solar visible light in the photocatalytic reduction of Cr(VI), surpassing the individual NMs.

However, the synthesized nano particle size of the agglomerated structure can be calculated from UV-vis DRS using a formula mentioned by ref. 46 in eqn (4)

$$d = \exp\left(3.55\frac{A_{\mathrm{LSPR}}}{A_{450}} - 3.11\right) \quad (4)$$

By using the above formula $ZnAgIn_5S_8$, SrGO, and $ZnAgIn_5S_8$/CdS/SrGO particle size diameters are calculated 9.41 nm, 7.38, and 6.55 nm respectively. As CdS grain size is spherical obtained from SEM images its particle diameter is calculated to be 46 nm by using the formula mentioned by[46] in eqn (5)

$$\lambda_{\mathrm{LSPR}} = 512 + 6.53\exp(0.0216d) \quad (5)$$

**3.1.4. Photoluminescence spectroscopy (PL) of the synthesized nanocomposite.** To study the degrees of photogenerated electron and hole pair recombination, the NMs were further analyzed using the photoluminescence (PL) spectroscopy technique. Fig. 3(b) illustrates the PL spectra of synthesized NMs. The Zn-$AgIn_5S_8$ NP peak is centered at 659 nm, which is in good agreement with the reported literature.[12] The CdS NPs exhibited a broad emission band in the range of 500–600 nm (centered at 551 nm), well supported by reported literature.[47] The emission peak of SrGO is observed at 763 nm; similar findings have also been reported in the literature.[48] The emission peak of Zn-$AgIn_5S_8$/CdS/SrGO is centered at 469 nm. It is observed that the intensity of the PL peak of the Zn-$AgIn_5S_8$/CdS/SrGO nanocomposite decreases as compared to the individual photocatalysts of Zn-$AgIn_5S_8$, CdS, and SrGO.

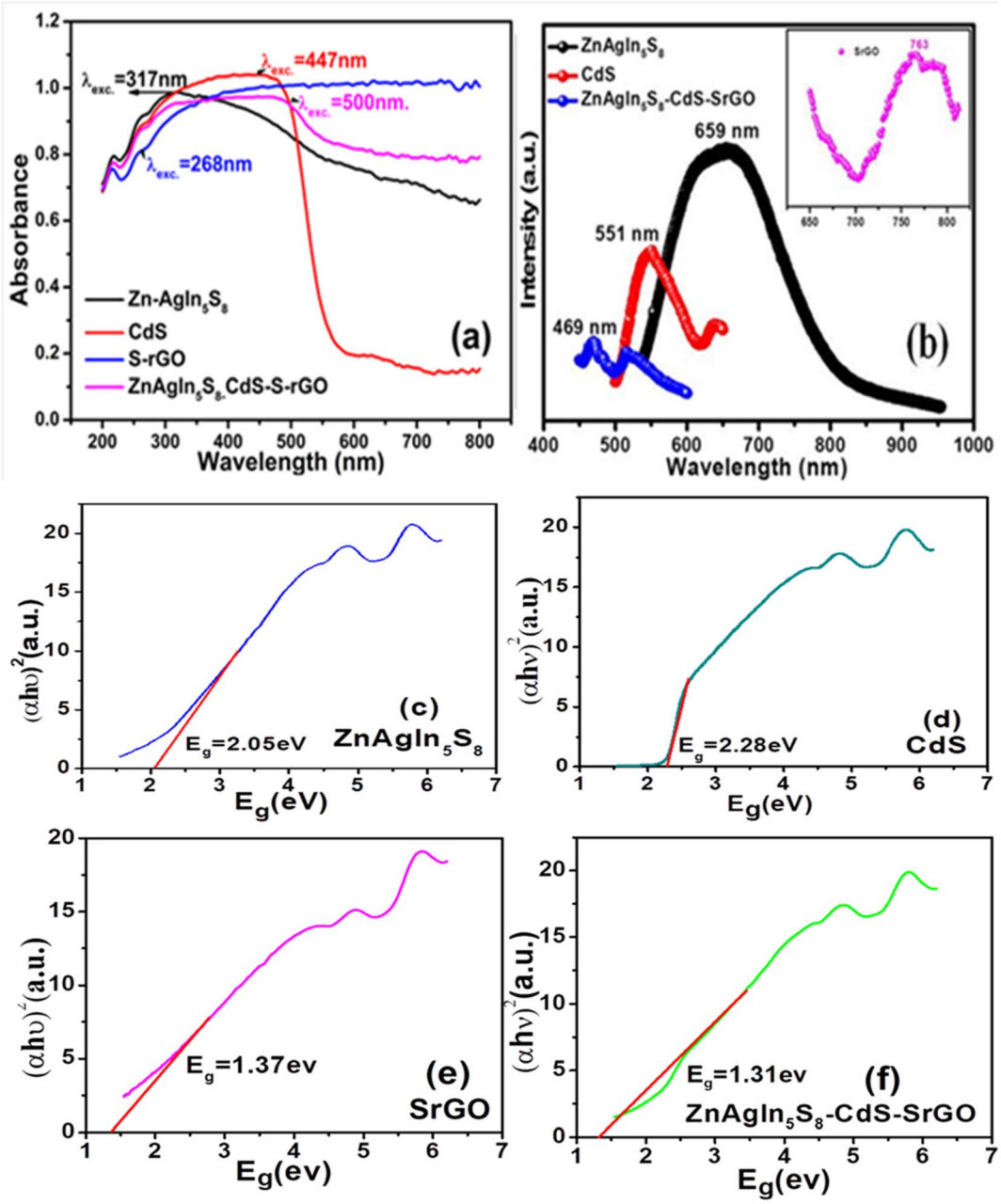


Fig. 3 (a) UV DRS study of Zn-$AgIn_5S_8$, CdS, Zn-$AgIn_5S_8$/CdS/SrGO NMs (b) PL spectra of Zn-$AgIn_5S_8$, CdS, SrGO, and Zn-$AgIn_5S_8$/CdS/SrGO nanocomposite. Tauc plot for calculating Bandgap energy of the synthesized NMs (c) Zn-$AgIn_5S_8$ (d) CdS (e) SrGO (f) Zn-$AgIn_5S_8$/CdS/SrGO nanocomposite.

This finding agrees with the universal concept of PL spectroscopy that the smaller the peak intensity, the higher the charge separation efficiency.[8,25]

**3.1.5. Raman spectroscopy of synthesized nanocomposite.** The structural, vibrational, and polymorphous characteristics of the NMs can be inferred by Raman spectroscopy. Polycrystalline or amorphous materials exhibit broad Raman peaks, whereas crystalline specimens display sharp bands.[49] Raman peaks broaden and shift downward due to the confinement effect of nanocrystalline materials. Additionally, tensile and compressive stresses have a noticeable impact on the Raman spectrum, leading to a shift towards longer wavelengths (redshift) or shorter wavelengths (blue shift).[50,51] Fig. 4(a) demonstrates the Raman spectra of $ZnAgIn_5S_8$ nanocomposite. Notably, there is a wide Raman peak at approximately 535 $cm^{-1}$, a feature exclusive to the Ag-doped samples, and it has been identified in the literature as the interfacial surface phonon mode.[52] Additionally, there are less prominent peaks at 117, 200, and 295 $cm^{-1}$, indicating the presence of ZnO–Ag, with these peaks being more prominent in the Zn–O samples deposited on the silver layer. The peaks observed at 117 $cm^{-1}$ corresponded to the $E_2$ (low) fundamental phonon modes of

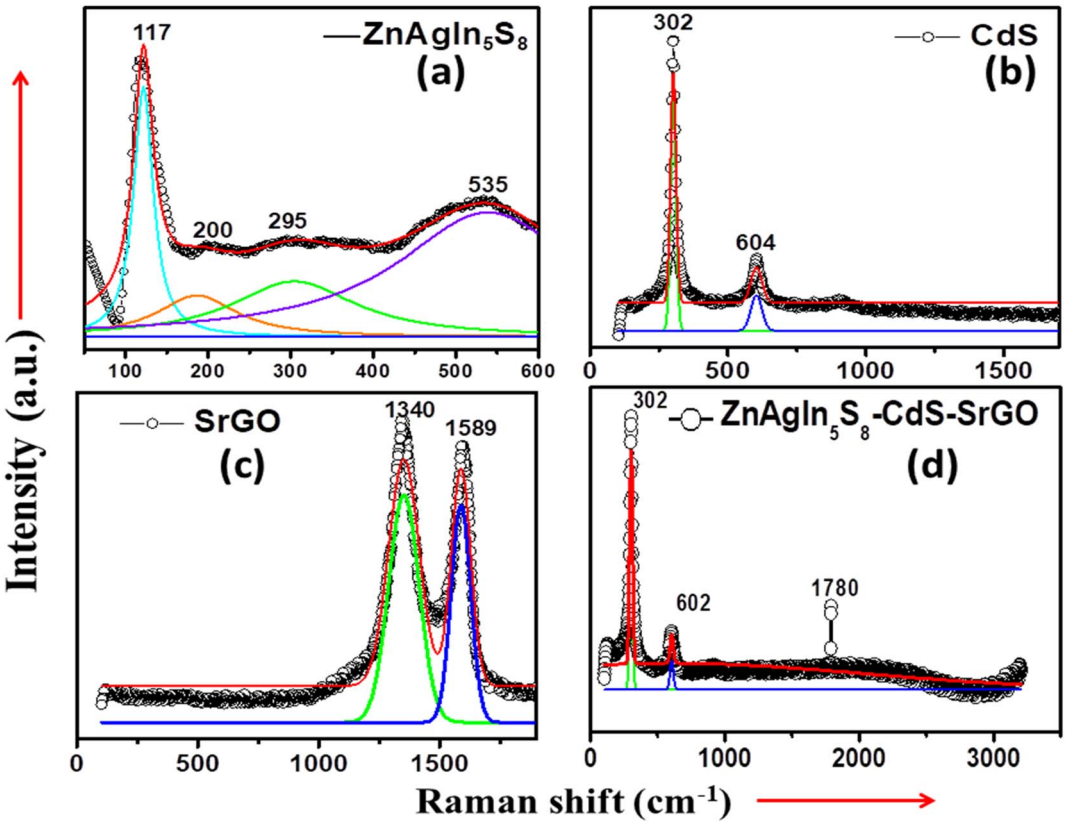


Fig. 4 Raman shift *vs.* Intensity of (a) Zn-$AgIn_5S_8$, (b) CdS, (c) SrGO, and (d) Zn-$AgIn_5S_8$/CdS/SrGO nanocomposite.

ZnO with a hexagonal wurtzite structure. The peak that appeared at 295 $cm^{-1}$ was assigned to $E_2$ (high)–$E_2$ (low) multiphonon scattering. The peaks at 200 $cm^{-1}$ correspond to sufficient doping of Ag on the surface of $ZnAgIn_5S_8$.[53] Fig. 4(b) demonstrates the Raman spectra of CdS NPs. From the figure, it can be seen that there are strong and wide peaks at approximately 302 $cm^{-1}$ and 604 $cm^{-1}$, corresponding to the fundamental optical phonon mode (LO) and the first overtone mode (2LO) of CdS NPs. These findings are consistent with prior reports in the literature.[54] Fig. 4(c) displays the Raman spectra of SrGO, with two distinct peaks occurring at 1340 $cm^{-1}$ and 1589 $cm^{-1}$. The band at 1340 $cm^{-1}$ can be attributed to the vibration of $sp^3$ carbon atoms, indicating the presence of defects and disorder in the SrGO structure. Conversely, the peak at 1589 $cm^{-1}$ is attributed to the vibration mode of $sp^2$ carbon atoms within the graphitic hexagonal lattice.[55,56] The D vibration band formed from a breathing mode of j-point photons of $A_{1g}$ symmetry seen at 1348.31 and 1340 $cm^{-1}$ for GO and SrGO, respectively. On the other hand, the G vibration band from first-order scattering of $E_{2g}$ phonons by $sp^2$ carbon appeared at 1594.19 and 1589 $cm^{-1}$ for GO and SrGO, respectively. Furthermore, the G vibration band was also contributed by the presence of the stretching C–C bond, which is common in all $sp^2$ carbon systems. The D band and G band in the Raman spectrum symbolize the disorder bands and the tangential bands, respectively.[57] In the case of SrGO, all observed peaks exhibit a slight shift to lower frequencies (redshift) and a narrowing of the peak width. This phenomenon is likely a consequence of structural reordering during the reduction and sulfonation processes. Fig. 4(d) illustrates the Raman spectra of the synthesized $ZnAgIn_5S_8$/CdS/SrGO nanocomposite. The presence of peaks at 302 and 602 $cm^{-1}$ is in good agreement with the previously described CdS and h-$In_2O_3$ structures.[58] The Raman signal of SrGO lies at ~1780 $cm^{-1}$ in the composite $ZnAgIn_5S_8$/CdS/SrGO. Further, the frequency range between 350 and 650 $cm^{-1}$ encompasses the primary Raman peaks associated with Zn-O. Therefore, it can be said that these Raman spectra peaks confirmed the XRD analysis results.

**3.1.6. FE-SEM analysis of the synthesized nanocomposite.** The FE-SEM characterization was performed to analyze the morphological structure size and distribution of the synthesized NMs.[8] The morphology of the Zn-$AgIn_5S_8$ is shown in Fig. 5(a), which demonstrates the nanoflower structure is composed of a multilayer sheet. Similar to observations reported in the literature.[59] The Ag, which is used for doping, reveals the agglomeration of round-shape particles with a particle size larger than that of Zn and well matched with reported literature.[60] The micrograph shown in Fig. 5(b) confirms the formation of CdS NPs and also substantiates the uniform globular-like morphology with a close enough uniform size of less than 50 nm and a similar result reported in the literature.[8] Fig. 5(c) demonstrates the FESEM image of SrGO. The SrGO displayed a networked, 3D porous, exfoliated, and corrugated architecture. Additionally, the elimination of oxygen-containing groups from the surface of GO during its

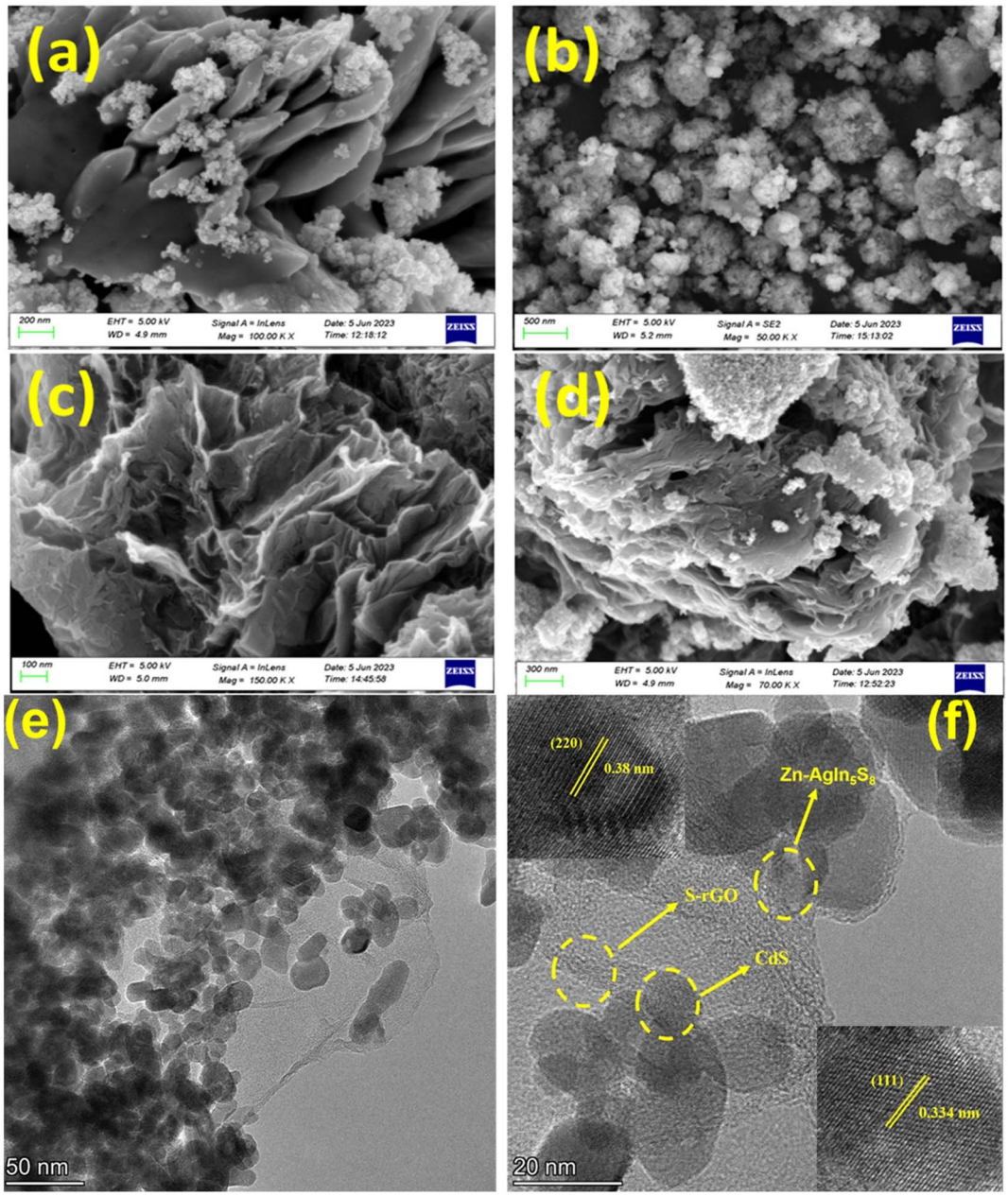


Fig. 5 FE-SEM micrographs of (a) Zn-$AgIn_5S_8$, (b) CdS, (c) SrGO, and (d) Zn-$AgIn_5S_8$/CdS/SrGO. (e) TEM image of Zn-$AgIn_5S_8$-CdS-S-rGO heterojunction, (f) HRTEM image of Zn-$AgIn_5S_8$-CdS-S-rGO heterojunction (inset: lattice fringes of Zn-$AgIn_5S_8$ and CdS).

reduction process results in an aggregated and corrugated structure, which is caused by the π–π stacking of the graphene molecules.[25] A similar observation is also reported in the literature.[61] In Fig. 5(d), from SEM images of Zn-$AgIn_5S_8$/CdS/SrGO nanocomposite, it is inferred that Zn-$AgIn_5S_8$ and CdS nanoparticles are uniformly distributed over the interconnected 3D porous, exfoliated, and corrugated structure of S-rGO, and thus confirm the formation of the nanocomposite.

The morphology of the ternary Zn-$AgIn_5S_8$–CdS–S-rGO heterojunction was examined by TEM. As shown in Fig. 5(e), S-rGO shows a transparent 2D nanosheet structure where both Zn-$AgIn_5S_8$ and CdS are spherical in shape. In addition, spherical-shaped Zn-$AgIn_5S_8$ and CdS of nearly 10–12 nm are uniformly distributed on the S-rGO nanosheets. The HRTEM image in Fig. 5(f) shows that the 0.38 nm lattice is clearly related to the (220) crystal plane of Zn-$AgIn_5S_8$, the 0.334 nm lattice is related to the (111) plane of CdS, and the 0.35 nm lattice spacing confirms the presence of S-rGO.[10,62] This result shows that the *in situ* hydrothermal approach is successful in loading the Zn-$AgIn_5S_8$ and CdS onto S-rGO nanosheets and that the inclusion of Zn-$AgIn_5S_8$ and CdS into S-rGO nanosheets has no effect on the lattice structure of the pure Zn-$AgIn_5S_8$ and CdS.

**3.1.7. EDX analysis of the synthesized nanocomposite.** Energy dispersive X-ray spectroscopy is a very popular technique for quantitative elemental analysis and determining the chemical composition of the NMs. The EDX spectrum, shown in

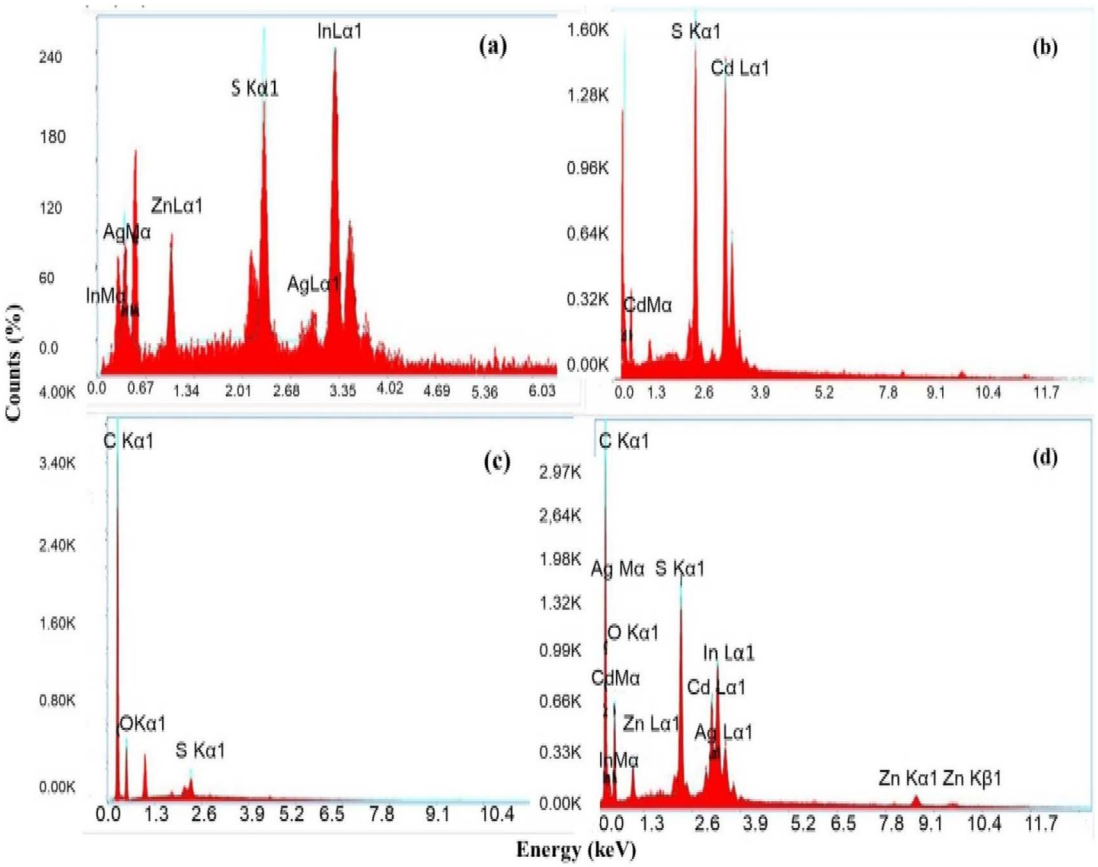


Fig. 6 EDX spectra of the synthesized nanomaterials (a) Zn-$AgIn_5S_8$, (b) CdS, (c) SrGO, and (d) Zn-$AgIn_5S_8$/CdS/S-rGO.

Fig. 6(a), confirms the presence of elements such as Zn, Ag, In, and S in the synthesized Zn-$AgIn_5S_8$ NMs. The Zn-$AgIn_5S_8$ NP compound has two primary elements, indium and sulfur. This may be deduced from the presence of two distinct peaks for each element with a near stoichiometric ratio. As Zn and Ag are both used for doping, their presence is minimal compared to In and S. Fig. 6(b) demonstrates the EDX spectra of the CdS NPs. From the figure, the presence of a stoichiometric ratio of Cd and S indicates the CdS NPs are successfully synthesized, and both Cd and S elements are uniformly distributed in the NPs. The EDX data of SrGO is shown in Fig. 6(c), which confirms the presence of C, O, and S elements in the NPs. Based on the EDX data, the amount of carbon in the SrGO is much greater than oxygen. As sulfur is used only as a doping agent, the presence of sulfur in SrGO is very minimal. Fig. 6(d) confirms the presence of elements like Zn, Ag, In, S, Cd, C, and O in the Zn-$AgIn_5S_8$/CdS/SrGO nanocomposite. It also ensures that the synthesized nanocomposite is in its pure form and that no other foreign elements are present in it.

### 3.2. Chromium reduction profile of the Zn-$AgIn_5S_8$/CdS/SrGO nanocomposite

Fig. 7(a) presents the Cr(VI) reduction profile under dark and visible light exposure conditions. It is evident that during the dark phase, the Cr(VI) reduction remains minimal, around 5–7%. In contrast, the Cr(VI) reduction activity by the bare SrGO and Zn-$AgIn_5S_8$ photocatalysts increases to almost 35% and 52%, respectively, at 40 mg $L^{-1}$ initial Cr(VI) under the illumination of visible light. Conversely, the Cr(VI) reduction activity is drastically improved with the formation of the Zn-$AgIn_5S_8$/CdS/SrGO nanocomposite. For instance, the Zn-$AgIn_5S_8$/CdS/SrGO nanocomposite shows maximum reduction efficiency as compared to the individual nanomaterials, *i.e.*, 100% in 40 mg $L^{-1}$ Cr(VI) in 180 min. Further, almost 85% of the Cr(VI) reduction was achieved by the Zn-$AgIn_5S_8$/CdS/SrGO nanocomposite at an initial Cr(VI) dose of 50 mg $L^{-1}$. Fig. 7(b) demonstrates the Cr(VI) reduction profile of the Zn-$AgIn_5S_8$/CdS/SrGO nanocomposite at varying Cr(VI) dosages from 25 to 50 mg $L^{-1}$. It is observed that maximum Cr(VI) reduction, *i.e.*, 100%, is observed in 25, 30, and 40 mg $L^{-1}$ of Cr(VI), where it drops to 85% when the initial concentration increases to 50 mg $L^{-1}$. In Fig. 7(b1) when the nanocomposite was exposed to dark conditions for 120 min, it showed no significant Cr(VI) reduction *i.e.* approximately 20% reductions at an initial dose of 40 mg $L^{-1}$ Cr(VI) which was taken as control. But when exposed to visible light irradiation for 120 min Cr(VI) reduction was enhanced up to 86.5%. Table 1 represents the comparative Cr(VI) reduction performance of various catalysts reported in the literature. From the table, it can be seen that Zn-$AgIn_5S_8$/CdS/SrGO nanocomposite is superior to many photocatalysts reported in the literature, such as ZnO-Ag-$BiVO_4$, ZnO/CdS/rGO, ZnO/PANI (polyaniline), rGO-$Sm_2MoO_6$-$TiO_2$, rGO/BiOI/ZnO,

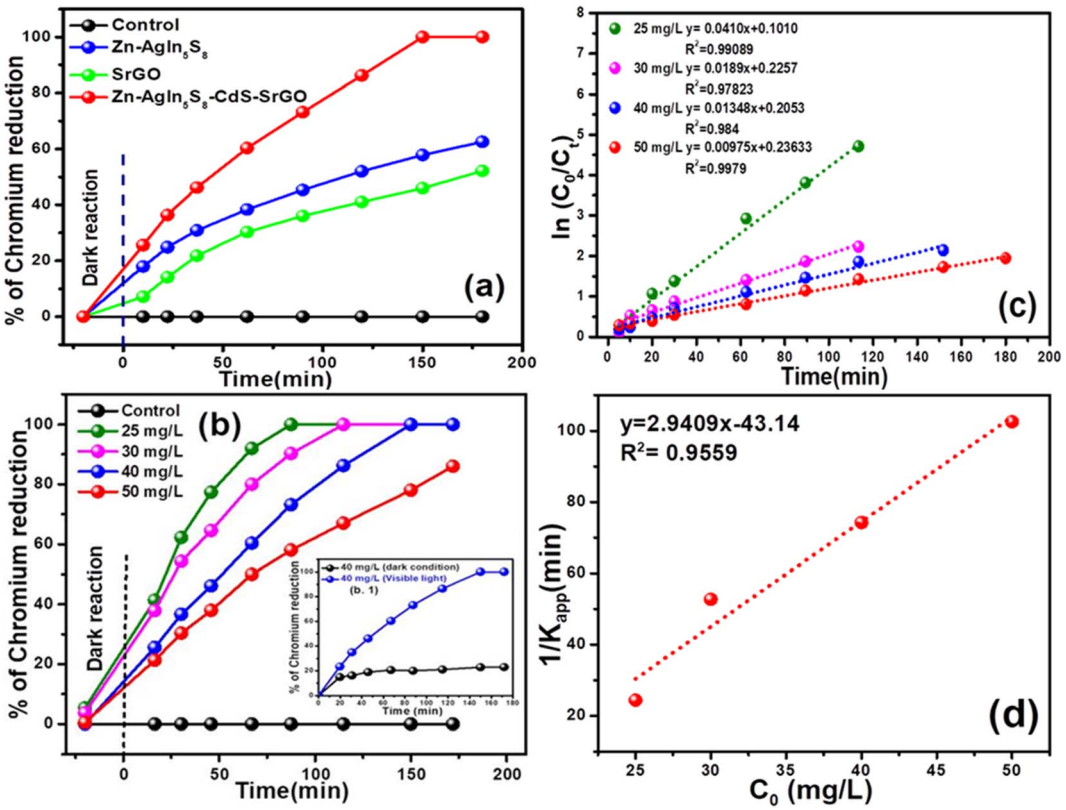


Fig. 7 (a) Demonstration of adsorption and Cr(VI) reduction profiles of individual nanomaterial and nanocomposite (b) demonstration of adsorption and Cr(VI) reduction profile of nanocomposite at varying initial Cr(VI) dose (c) kinetic of Cr(VI) reduction by the nanocomposite with varying its initial concentration (d) pseudo-first-order kinetic for variation of reciprocal of apparent rate constant *versus* different initial concentrations of Cr(VI).

rGO-CdS-MnOx (GCM), $AgIn_5S_8/ZnIn_2S_4$ and $AgInS_2/AgIn_5S_8$ QDs photocatalyst.

### 3.3. Kinetics of photocatalytic reduction of Cr(VI) using Zn-$AgIn_5S_8$/CdS/SrGO nanocomposite

The photocatalytic reactions occurring at the interface between liquids and solids can be effectively deduced by applying the Langmuir–Hinshelwood kinetic model (L–H model). Typically, this model is applied to examine the correlation between pollutant removal rates and their initial concentrations. The Cr(VI) removal rate can be expressed using the L–H model as follows:

$$r = -\frac{dc}{dt} = \frac{CKk_r}{1 + KC} \quad (6)$$

In this context, the Cr(VI) reduction rate (mg $min^{-1}$) is denoted as '*r*'. *K* stands for the Langmuir–Hinshelwood equilibrium constant; '*t*' signifies the duration of light exposure in min; the photocatalysis rate constant is expressed as '$k_r$' (mg $L^{-1}$ $min^{-1}$), and '*C*' corresponds to the Cr(VI) dose in mg $L^{-1}$ at a time '*t*'. By integrating eqn (6) over the light irradiation time '*t*' and the concentration of Cr(VI) 'Ct', the equation can be expressed in the following ways:

$$t = \left[\frac{1}{Kk_r}\right]\ln\left[\frac{C_0}{C_r}\right] + \frac{C_0 - C_r}{k_r} \quad (7)$$

where ($C_0$) stands for the initial dose of Cr(VI) and (Ct) is the equilibrium level of Cr(VI) at time *t*, respectively. The factor $K_c$ can be ignored when $C_0$ is relatively small, resulting in a linear apparent first-order kinetic model as shown in the equation below.[8,25]

$$\ln\left(\frac{C_0}{C_t}\right) = k_r K t = K_{app} t \quad (8)$$

In eqn (8), '$K_{app}$' represents the apparent first-order rate constant ($min^{-1}$). Fig. 7(c) displays a plot of $\ln(C_0/C_t)$ against time ($t$), with the slope of the plot representing the apparent rate constant ($K_{app}$). The experimental data for Cr(VI) reduction using the nanocomposite are very well fitted with the pseudo-first-order kinetic model, with a high correlation coefficient value ($R^2 \geq 0.97$). From the figure, it can be deduced that the $K_{app}$ value for Zn-$AgIn_5S_8$/CdS/SrGO ($K_{app}$ = 0.0114 $min^{-1}$) is approximately 1.67 and 1.60 times higher than that of pure Zn-$AgIn_5S_8$ ($K_{app}$ = 0.0068 $min^{-1}$) and SrGO ($K_{app}$ = 0.0071 $min^{-1}$), respectively. The L–H kinetic model can be simplified further, as shown below.

$$\frac{1}{K_{app}} = \frac{1}{k_r K} + \frac{C_0}{k_r} \quad (9)$$

Fig. 7(d) illustrates the graph between the initial Cr(VI) doses ($C_0$) *versus* $1/K_{app}$. The slope and intercept of the linear plot

Table 1 Comparison of the Cr(VI) reduction efficiency of the Zn-$AgIn_5S_8$/CdS/SrGO catalyst with reports in the literature

| Sl. no | Photocatalyst | Synthesis method | Experimental condition | Initial Cr(VI) conc. mg $L^{-1}$ | Inference of photocatalytic degradation | Reference |
|---|---|---|---|---|---|---|
| 1 | ZnO-Ag-$BiVO_4$ | Hydrothermal | Visible light | 20 | 97% in 70 min | 69 |
| 2 | ZnO/CdS/rGO | Hydrothermal | Visible light | 10 | 100% in 30 min | 21 |
| 3 | rGO/BiOI/ZnO | Hydrothermal | Visible light | 10 | 92% 180 min | 70 |
| 4 | ZnO/PANI (polyaniline) | Low temperature (80 °C) solution | Visible light | 20 | 98% in 120 min | 71 |
| 5 | rGO-$Sm_2MoO_6$-$TiO_2$ | Hydrothermal | Visible light | 10 | 96% in 70 min | 72 |
| 6 | rGO-CdS-MnOx (GCM) | Chemical precipitation | Visible light | 20 | 95.49% in 21 min | 9 |
| 7 | $AgIn_5S_8$/$ZnIn_2$ S4 | Hydrothermal | Visible light | 10 | 88.5% in 300 min | 73 |
| 8 | $AgInS_2$/$AgIn_5S_8$ QDs | Hydrothermal | Visible light | 10 | 97.7% in 20 min | 74 |
| 9 | Zn-$AgIn_5S_8$/CdS/SrGO | Hydrothermal | Visible light | 50 | 85% in 180 min | This work |

represent the photocatalytic rate constant ($k_r$) and L–R adsorption equilibrium constant ($K$), respectively. The experimental data fitted remarkably well with the L–R kinetic model, with a very high regression coefficient value ($R^2 = 0.95$). The present investigation estimated a photocatalytic rate constant ($K_r$) of 0.34 $min^{-1}$ and an L–R adsorption constant of −0.068 mg $L^{-1}$. In the present study, the photocatalytic rate constant ($K_r$) value is found to be superior to many reports in the literature, such as 0.106 $min^{-1}$ (ref. 21) and 0.106 $min^{-1}$.[36]

### 3.4. Recycle and separation of Zn-$AgIn_5S_8$/CdS/SrGO catalyst

The recycling ability of the spent Zn-$AgIn_5S_8$/CdS/SrGO photocatalyst was tested with 10% $HNO_3$. After removal of Cr(VI) by the Zn-$AgIn_5S_8$/CdS/SrGO photocatalytic system, the nanocomposite was soaked in a 10% $HNO_3$ solution for 1 h, followed by washing with deionized water several times and dried in a desiccator.[63] The regenerated Zn-$AgIn_5S_8$/CdS/SrGO photocatalyst was freshly evaluated for the removal of Cr(VI) with an initial dose of 40 mg $L^{-1}$ under similar experimental conditions. The Cr(VI) removal efficiencies in the 1st, 2nd, 3rd, 4th, and 5th cycles are calculated to be 100%, 86%, 82%, 75%, and 72%, respectively. This result demonstrates that the Zn-$AgIn_5S_8$/CdS/SrGO catalyst can be recycled conveniently and economically.

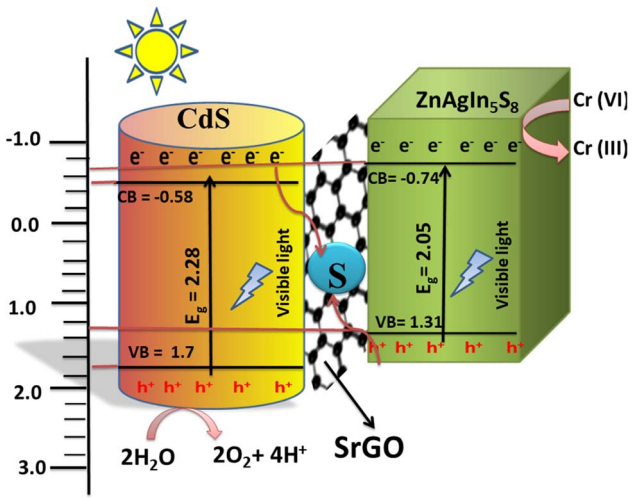


Scheme 2 Photocatalytic mechanism of Cr(VI) reduction using Zn-$AgIn_5S_8$/S-rGO/CdS nanocomposite.

### 3.5. Mechanism of photoreduction of Cr(VI) C by Zn-$AgIn_5S_8$/CdS/SrGO nanocomposite

Upon visible light irradiation, the electrons from both Zn-$AgIn_5S_8$ and CdS photocatalysts are excited to their respective CBs and form holes in the VB as shown in Scheme 2. Since the CB potential of CdS is more negative (−0.46 to −0.58 eV) than that of S rGO (−0.08 eV),[64–66] the photogenerated electrons from the CB of CdS can easily transfer to the S-doped rGO (−0.08 eV) nanoparticles through the Schottky barrier. Meanwhile, the holes in the VB of Zn-$AgIn_5S_8$ (VB = 1.31–1.54 eV) also transfer to the S-doped rGO nanoparticles, due to the more positive potentiation of Zn-$AgIn_5S_8$ than S-rGO.[12,15,66] The movement of the e− follows the Z-scheme mechanism from the CB of CdS towards S-doped rGO and recombines with the VB holes of Zn-$AgIn_5S_8$, as shown in Scheme 2. The VB holes of Zn-$AgIn_5S_8$ and CB electrons of CdS were thus annihilated in the S-doped rGO, effectively inhibiting electron–hole pair recombination in both Zn-$AgIn_5S_8$ and CdS, consequently enhancing interfacial charge transfer and redox potential. In addition, the S-doped rGO provides a high surface area, together with the presence of the π–π conjugation effect and $SP^2$ hybridization, drastically improving the efficient transfer of photo-induced charge carriers between CdS and Zn-$AgIn_5S_8$. The photogenerated electrons at the CB of Zn-$AgIn_5S_8$ can reduce the Cr(VI) ion to the Cr(III) ion since the ECB of Zn-$AgIn_5S_8$ (−0.74 to 0.76 eV)[12,15] is more negative than the reduction potential of Cr(VI)/Cr(III) (1.33 eV *vs.* NHE).[67] Simultaneously, the photogenerated holes at the VB of CdS can oxidize $H_2O$ to $O_2$ and $2H^+$ since the EVB of CdS (1.64–2.1 eV) is more positive than the reduction potential of $O_2/H_2O$ (1.23 eV *vs.* NHE).[64,65,68] The reaction steps are provided as follows:

$$\text{Zn-AgIn}_5\text{S}_8/\text{CdS} + h\nu\ (\text{visible}) \rightarrow \text{Zn-AgIn}_5\text{S}_8\ (\text{eCB}^-) + \text{CdS}\ (\text{h}_{\text{VB+}}) \quad (10)$$

$$2\text{H}_2\text{O} + \text{CdS}\ (4\text{h}_{\text{VB+}}) \rightarrow \text{O}_2 + 4\text{H}^+ \quad (11)$$

$$\text{Cr}_2\text{O}_7^{2-} + 14\text{H+} + \text{Zn-AgIn}_5\text{S}_8\ (6\text{eCB}^-) \rightarrow 2\text{Cr(III)} + 7\text{H}_2\text{O} \quad (12)$$

## 4. Conclusion

Zn-$AgIn_5S_8$/CdS/SrGO nanocomposite was successfully prepared by employing a hydrothermal technique. The Zn-

$AgIn_5S_8$ NPs are well dispersed on the nanoflower S-doped rGO, as shown in the FESEM image, leading to an intimate interface structure. The introduction of $Ag^{2+}$ plasmonic materials extended the light absorption range and stabilized the photocatalyst. To further improve the efficient interface contact between Zn-$AgIn_5S_8$ and CdS, the catalytic surface area, electrical conductivity, and minimized rate of electron and hole pair recombination, the Zn-$AgIn_5S_8$/CdS Z-scheme heterojunction was loaded onto S-doped rGO. When exposed to solar illumination, the Zn-$AgIn_5S_8$/CdS/SrGO nanocomposite achieved a 100% Cr(VI) reduction at an initial concentration of 40 mg $L^{-1}$ and an 85% Cr(VI) reduction at an initial concentration of 50 mg $L^{-1}$ within 180 min. The experimental data for Cr(VI) reduction using the nanocomposite fit with the pseudo-first-order kinetic model has a high correlation coefficient ($R^2 \geq 0.97$) and the $K_{app}$ value for Zn-$AgIn_5S_8$/CdS/SrGO ($K_{app} = 0.0114$ $min^{-1}$) is 1.67 times greater than bare Zn-$AgIn_5S_8$. Moreover, Zn-$AgIn_5S_8$/CdS/SrGO heterojunctions show excellent reusability up to 4 cycles. This study provides a reasonable design of suitable band matching to adjust the charge transfer characteristics by constructing a Z-scheme heterojunction for efficient utilization of visible light for the removal of Cr(VI) from wastewater.

## Data availability

The data supporting this article can be found at Mandalay data set DOI: **https://www.doi.org/10.17632/rnwf45wg4d.1**.

## Author contributions

Soumya Mishra: investigation, methodology, formal analysis, validation, data curation, writing – original draft, writing – review & editing, Naresh Kumar Sahoo: conceptualization, visualization, investigation, supervision, resources, writing – original draft, formal analysis, funding acquisition. Satyanjib Sahoo: investigation, formal data curation, formal analysis, writing – review & editing. Prasanta Kumar Sahoo: conceptualization, investigation, formal analysis, visualization, review & editing. Prangya Ranjan Rout: conceptualization, investigation, formal analysis, visualization, review & editing. Goutam Rath: investigation, formal analysis, writing – original draft.

## Conflicts of interest

The authors declare that they have no known competing financial interests or personal relationships that could have appeared to influence the work reported in this paper.

## Acknowledgements

The authors acknowledge the financial support received from Department of Biotechnology, Ministry of Science & Technology, India (SAN No. 102/IFD/SAN/3612/2016-2017), for carrying out this research work.

## References

1 P. Sane, S. Chaudhari, P. Nemade and S. Sontakke, *J. Environ. Chem. Eng.*, 2018, **6**, 68–73.
2 S. Singh, A. G. Anil, S. Khasnabis, V. Kumar, B. Nath, V. Adiga, T. S. S. K. Naik, S. Subramanian, V. Kumar, J. Singh, *et al.*, *Environ. Res.*, 2022, **203**, 111891.
3 M. Abinaya, K. Govindan, M. Kalpana, K. Saravanakumar, S. L. Prabavathi, V. Muthuraj and A. Jang, *J. Hazard. Mater.*, 2020, **397**, 122885.
4 Q. Cheng, C. Wang, K. Doudrick and C. K. Chan, *Appl. Catal., B*, 2015, **176**, 740–748.
5 M. Yu, J. Shang and Y. Kuang, *J. Mater. Sci. Nanotechnol.*, 2021, **91**, 17–27.
6 A. Saravanan, S. Karishma, S. Jeevanantham, S. Jeyasri, A. R. Kiruthika, P. S. Kumar and P. R. Yaashikaa, *Surf. Interfaces*, 2020, **20**, 100520.
7 A. Saravanan, P. S. Kumar, D.-V. N. Vo, P. R. Yaashikaa, S. Karishma, S. Jeevanantham, B. Gayathri and V. D. Bharathi, *Environ. Chem. Lett.*, 2021, **19**, 441–463.
8 S. K. Sahoo, A. A. Das, D. Deka, B. Naik and N. K. Sahoo, *J. Mol. Liq.*, 2021, **339**, 116721.
9 K. Xuan, T. Li and Y. Hao, *Ceram. Int.*, 2024, **50**, 3701–3709.
10 D. Zhang, W. Cao, B. Mao, Y. Liu, F. Li, W. Dong, T. Jiang, Y.-C. Yong and W. Shi, *Ind. Eng. Chem. Res.*, 2020, **59**, 16249–16257.
11 A. Jiang, H. Guo, S. Yu, F. Zhang, T. Shuai, Y. Ke, P. Yang and Y. Zhou, *Appl. Catal., B*, 2023, **332**, 122747.
12 Y. Yang, B. Mao, G. Gong, D. Li, Y. Liu, W. Cao, L. Xing, J. Zeng, W. Shi and S. Yuan, *Int. J. Hydrogen Energy*, 2019, **44**, 15882–15891.
13 H. Targhan, A. Rezaei, A. Aliabadi, A. Ramazani, Z. Zhao, X. Shen and H. Zheng, *Sci. Rep.*, 2024, **14**, 530.
14 Y. Liu, Q. Zhang, B. Yang, J. Xu, Y. Yan and J. He, *J. Mater. Sci.: Mater. Electron.*, 2019, **30**, 15257–15266.
15 D. Zhang, B. Mao, D. Li, Y. Liu, F. Li, W. Dong, T. Jiang and W. Shi, *Chem. Eng. J.*, 2021, **417**, 128275.
16 X.-B. Li, C.-H. Tung and L.-Z. Wu, *Nat. Rev. Chem*, 2018, **2**, 160–173.
17 G. Gong, Y. Liu, B. Mao, B. Wang, L. Tan, D. Li, Y. Liu and W. Shi, *RSC Adv.*, 2016, **6**, 99023–99033.
18 J. Yang, Z. Yang, K. Yang, Q. Yu, X. Zhu, H. Xu and H. Li, *Chin. J. Catal.*, 2023, **44**, 67–95.
19 L. Jie, X. Gao, X. Cao, S. Wu, X. Long, Q. Ma and J. Su, *Mater. Sci. Semicond. Process.*, 2024, **176**, 108288.
20 J. Yang, L. Li, J. Wang, H. Zhang, L. Wei and X. Yang, *Opt. Mater.*, 2024, **148**, 114963.
21 Y. Zhao, L. Li, Y. Zuo, G. He, Q. Chen, Q. Meng and H. Chen, *Chemosphere*, 2022, **286**, 131738.
22 R. Kumar, A. Sudhaik, A. A. P. Khan, P. Raizada, A. M. Asiri, S. Mohapatra, S. Thakur, V. K. Thakur and P. Singh, *J. Ind. Eng. Chem.*, 2022, **106**, 340–355.
23 D. S. Pattanayak, J. Mishra, J. Nanda, P. K. Sahoo, R. Kumar and N. K. Sahoo, *J. Environ. Manage.*, 2021, **297**, 113312.
24 Y. Dai, J. Ding, J. Li, Y. Li, Y. Zong, P. Zhang, Z. Wang and X. Liu, *Nanomaterials*, 2021, **11**, 202.

25 S. Bhattacharya, A. A. Das, G. C. Dhal, P. K. Sahoo, A. Tripathi and N. K. Sahoo, *J. Environ. Manage.*, 2022, **302**, 114022.
26 D. He, W. Zhao, P. Li, S. Sun, Q. Tan, K. Han, L. Liu, L. Liu and X. Qu, *J. Alloys Compd.*, 2019, **773**, 11–20.
27 Z. Tian, J. Li, G. Zhu, J. Lu, Y. Wang, Z. Shi and C. Xu, *Phys. Chem. Chem. Phys.*, 2016, **18**, 1125–1130.
28 T. Madrakian, S. Maleki and A. Afkhami, *Sens. Actuators, B*, 2017, **243**, 14–21.
29 M. Duraivel, S. Nagappan, B. Balamuralitharan, S. Selvam, S. N. Karthick, K. Prabakar, C.-S. Ha and H.-J. Kim, *New J. Chem.*, 2018, **42**, 11093–11101.
30 G. Venkatesan and T. Subramani, *Indian J. Geo-Mar. Sci.*, 2019, **48**, 528–534.
31 P. Makuła, M. Pacia and W. Macyk, *J. Phys. Chem. Lett.*, 2018, **9**, 6814–6817.
32 M. H. K. AL-Mamoori, D. K. Mahdi and S. M. Alshrefi, *AIP Conf. Proc.*, 2018, **1968**, 030011.
33 B. S. Rao, B. R. Kumar, V. R. Reddy, T. S. Rao and G. Chalapathi, *Chalcogenide Lett.*, 2011, **8**, 177–185.
34 M. Brahmayya, S.-Y. Suen and S. A. Dai, *J. Taiwan Inst. Chem. Eng.*, 2018, **83**, 174–183.
35 M. Toumi, N. Bouguila, B. Tiss, C. Dias, R. C. Veloso, M. Kraini, J. Ventura and S. Alaya, *Solid State Sci.*, 2022, **133**, 107021.
36 A. Alsulamei and A. Timoumi, *Opt. Mater.: X*, 2022, **15**, 100176.
37 S. Gayathri, O. S. N. Ghosh, S. Sathishkumar, S. Sudhakara, J. Jayaramudu, S. S. Ray and A. K. Viswanath, *Appl. Sci. Lett.*, 2015, **1**(1), 8–13.
38 G. Nagaraju, S. A. Prashanth, M. Shastri, K. V Yathish, C. Anupama, D. Rangappa, *et al.*, *Mater. Res. Bull.*, 2017, **94**, 54–63.
39 H. S. Mahdi, A. Parveen, S. Agrawal and A. Azam, *AIP Conf. Proc.*, 2017, **1832**, 050012.
40 X. Zhao, J. Zhang, L. Shi, M. Xian, C. Dong and S. Shuang, *RSC Adv.*, 2017, **7**, 42159–42167.
41 S. R. K. Pandian, V. Deepak, K. Kalishwaralal and S. Gurunathan, *Enzyme Microb. Technol.*, 2011, **48**, 319–325.
42 N. Susha, K. Nandakumar and S. S. Nair, *RSC Adv.*, 2018, **8**, 11330–11337.
43 S. Hassanpoor and E. Tamri, *J. Alloys Compd.*, 2023, **932**, 167711.
44 N. E. Fard, R. Fazaeli and R. Ghiasi, *Chem. Eng. Technol.*, 2016, **39**, 149–157.
45 B. D. Ossonon and D. Bélanger, *RSC Adv.*, 2017, **7**, 27224–27234.
46 A. G. Shard, R. C. Schofield and C. Minelli, in *Characterization of Nanoparticles*, Elsevier, 2020, pp. 185–196.
47 T. R. Gurugubelli, R. Ravikumar and R. Koutavarapu, *Catalysts*, 2022, **12**, 84.
48 D. A. Bala, H. Ali, D. Eli and T. Yunana, *FUDMA J. Sci.*, 2019, **3**, 226–231.
49 V. Singh, P. K. Sharma and P. Chauhan, *Mater. Chem. Phys.*, 2010, **121**, 202–207.
50 B. Ahmed, S. Kumar, S. Kumar and A. K. Ojha, *J. Alloys Compd.*, 2016, **679**, 324–334.
51 P. Nandakumar, C. Vijayan, M. Rajalakshmi, A. K. Arora and Y. Murti, *Phys. E*, 2001, **11**, 377–383.
52 B. Jusserand, D. Paquet and F. Mollot, *Phys. Rev. Lett.*, 1989, **63**, 2397.
53 E. A. Alzahrani, A. Nabi, M. R. Kamli, S. M. Albukhari, S. A. Althabaiti, S. A. Al-Harbi, I. Khan and M. A. Malik, *Water*, 2023, **15**, 384.
54 D. S. Chuu, C. M. Dai, W. F. Hsieh and C. T. Tsai, *J. Appl. Phys.*, 1991, **69**, 8402–8404.
55 A. C. Ferrari, J. C. Meyer, V. Scardaci, C. Casiraghi, M. Lazzeri, F. Mauri, S. Piscanec, D. Jiang, K. S. Novoselov, S. Roth, *et al.*, *Phys. Rev. Lett.*, 2006, **97**, 187401.
56 J. Ji, G. Zhang, H. Chen, S. Wang, G. Zhang, F. Zhang and X. Fan, *Chem. Sci.*, 2011, **2**, 484–487.
57 N. M. S. Hidayah, W.-W. Liu, C.-W. Lai, N. Z. Noriman, C.-S. Khe, U. Hashim and H. C. Lee, *AIP Conf. Proc.*, 2017, **1892**, 150002.
58 D. Yu, S.-H. Yu, S. Zhang, J. Zuo, D. Wang and Y. T. Qian, *Adv. Funct. Mater.*, 2003, **13**, 497–501.
59 G.-G. Zheng, X. Lin, Z.-X. Wen, Y.-H. Ding, R.-H. Yun, G. Sharma, A. Kumar and F. J. Stadler, *J. Compos. Sci.*, 2023, **7**, 280.
60 L. Buengkitcharoen, S. Amnuaypanich, S. Naknonhan, S. Loiha, N. Patdhanagul, A. Makdee and S. Amnuaypanich, *Sci. Rep.*, 2023, **13**, 12173.
61 M. Q. Khan, P. Kumar, R. A. Khan, K. Ahmad and H. Kim, *Inorganics*, 2022, **10**, 218.
62 M. Fu, Q. Jiao and Y. Zhao, *RSC Adv.*, 2014, **4**, 23242–23250.
63 S. C. Xu, Y. X. Zhang, S. S. Pan, H. L. Ding and G. H. Li, *J. Hazard. Mater.*, 2011, **196**, 29–35.
64 G. Sun, J. Zhang, B. Cheng, H. Yu, J. Yu and J. Xu, *Chem. Eng. J.*, 2023, **476**, 146818.
65 F. Dong, L. Qin, T. Zhang, X. Li and S.-Z. Kang, *Int. J. Hydrogen Energy*, 2023, **48**, 13877–13889.
66 X. Dong, K. Wu, W. Zhu, P. Wu, J. Hou, Z. Wang, R. Li, J. Wu, Z. Liu and X. Guo, *J. Mater. Sci.*, 2019, **54**, 7834–7849.
67 J. Luo, X. Zhou, X. Ning, L. Zhan, L. Ma, X. Xu, Z. Huang and J. Liang, *New J. Chem.*, 2017, **41**, 845–856.
68 Z. Li, B. Liu, X. Zhang, C. Zhang, Y. Bai, J. Liu, Y. Wang, S. Yang, R. Li and C. Fan, *Sustainable Energy Fuels*, 2024, **8**, 262–271.
69 A. Raja, P. Rajasekaran, B. Vishnu, K. Selvakumar, J. Y. Do, M. Swaminathan and M. Kang, *Sep. Purif. Technol.*, 2020, **252**, 117446.
70 L. Yang, C. Xu, F. Wan, H. He, H. Gu and J. Xiong, *Mater. Res. Bull.*, 2019, **112**, 154–158.
71 C. Bao, M. Chen, X. Jin, D. Hu and Q. Huang, *J. Mol. Liq.*, 2019, **279**, 133–145.
72 A. Raja, P. Rajasekaran, K. Selvakumar, M. Arivanandhan, S. Asath Bahadur and M. Swaminathan, *ACS Omega*, 2020, **5**, 6414–6422.
73 M. Wu, N. Xu, B. Chen, J. Yang, M. Shen, Q. Li, M. Li, W. Liu, J. Lian and R. Wang, *J. Environ. Chem. Eng.*, 2024, **12**, 112880.
74 C. Lan, L. Meng and N. Xu, *Colloids Surf., A*, 2022, **632**, 127762.